IOP Publishing Smart Materials and Structures
Smart Mater. Struct. **26** (2017) 125020 (12pp) https://doi.org/10.1088/1361-665X/aa95af

A computationally efficient technique to model depth, orientation and alignment via ray tracing in acoustic power transfer systems

David B Christensen, Hamid Basaeri and Shad Roundy

University of Utah, Salt Lake City, UT, United States of America

E-mail: dave.christensen@utah.edu

Received 27 June 2017, revised 4 October 2017
Accepted for publication 24 October 2017
Published 9 November 2017

Abstract

In acoustic power transfer systems, a receiver is displaced from a transmitter by an axial depth, a lateral offset (alignment), and a rotation angle (orientation). In systems where the receiver's position is not fixed, such as a receiver implanted in biological tissue, slight variations in depth, orientation, or alignment can cause significant variations in the received voltage and power. To address this concern, this paper presents a computationally efficient technique to model the effects of depth, orientation, and alignment via ray tracing (DOART) on received voltage and power in acoustic power transfer systems. DOART combines transducer circuit equivalent models, a modified version of Huygens principle, and ray tracing to simulate pressure wave propagation and reflection between a transmitter and a receiver in a homogeneous medium. A reflected grid method is introduced to calculate propagation distances, reflection coefficients, and initial vectors between a point on the transmitter and a point on the receiver for an arbitrary number of reflections. DOART convergence and simulation time per data point is discussed as a function of the number of reflections and elements chosen. Finally, experimental data is compared to DOART simulation data in terms of magnitude and shape of the received voltage signal.

Keywords: ultrasonic transducer, wireless power transfer, implantable devices, DOART, acoustic power transfer, energy harvesting, implantable medical devices

(Some figures may appear in colour only in the online journal)

Introduction

Acoustic power transfer has gained increased interest in the last few years in the research community because of its application to implantable medical devices (IMD). A review of acoustic power transfer for the IMD field can be found in a recent review by Basaeri [1]. IMD devices are typically small, on the order of a cm or less, and have either a diagnostic or therapeutic function. Proposed acoustic power transfer systems used to wirelessly power IMDs are comprised of a transmitter (TX) and a receiver (RX) (typically piezoelectric) separated by tissue. The TX transduces electrical power to acoustic power and emits this acoustic power through tissue to power an RX implanted in the tissue. The RX transduces the acoustic power to electrical power to either charge or directly power the IMD that is attached to the RX.

Acoustic power transfer systems are commonly modeled using a network equivalent model such as Mason's model or the KLM model [2–10]. Such models assume an axially aligned TX and RX of the same diameter separated by a homogeneous medium and do not account for beam spreading. While network equivalent models are efficient and useful for quick and versatile modeling of power in a 1D system, more advanced models are needed to model effects such as beam spreading, TX and RX of differing diameters, and RX alignment and orientation. These more advanced models include finite difference

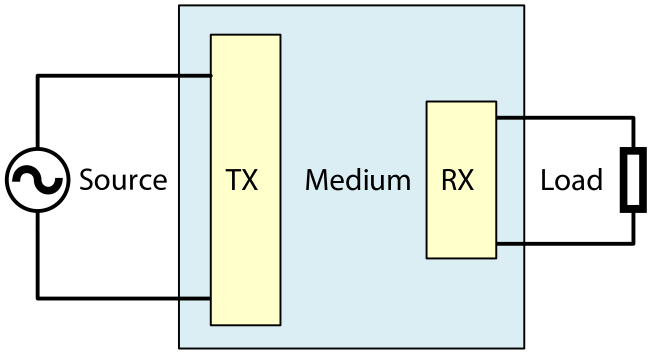

Figure 1. Block diagram of main components of DOART system: source, TX, medium, RX, and load.

and finite elements. These modeling techniques have also been frequently used in literature [4, 6–9, 11–14] and are typically accessed via commercial software in such programs as COMSOL and ANSYS. 2D axis-symmetric finite element models can model beam spreading and TX and RX of differing diameters. 3D finite element models are required to further model alignment and orientation. As rule of thumb, the number of elements needed to accurately model the propagation of acoustic waves is 6 to 12 elements per smallest expected wavelength [15, 16]. This element density can lead to a long simulation time per data point (or point at which each simulation parameter has a single value), especially for 3D elements and transducers that operate at high frequencies, have large diameters, or have a large separation distance (depth). When performing parameter sweeps, such as analyzing RX voltage/power as a function of RX placement, load, diameter, and frequency, the compounded number of data points can be computationally expensive to simulate. To reduce simulation time while still being able to model beam spreading, RX and TX of differing diameters, and RX alignment and orientation, a technique that models the effect of Depth, Orientation, and Alignment, via Ray Tracing (DOART) was developed and is presented in this paper. DOART treats acoustic waves as rays in the frequency domain and uses ray tracing to simulate reflections between 3D TX and RX geometries. It accounts for beam spreading and absorption and can handle TX and RX of differing diameters in 3D space with 3 degrees of freedom.

The purpose of this paper is to introduce the DOART modeling technique. This paper is organized as follows: (1) DOART system is presented and associated subsystems are explained. (2) Modified Huygens principle formulation for calculating pressure from the TX face is presented. (3) Reflected Grid Method to model pressure reflections is presented and working mathematical equations are developed. (4) Convergence and simulation time of DOART are discussed (5) Experimental setup is described and simulation data from DOART is compared to experimental data in terms of magnitude and shape.

DOART system

The DOART system is comprised of five sub-systems: source, TX, medium, RX, and load as shown in figure 1. The source is a sinusoidal electrical AC voltage source with an internal series-connected source impedance (typically 50 ohms) that powers the TX in continuous-wave mode. The TX and RX are acoustic transducers. The medium is a homogenous material. Note that only compression waves are considered in this work. So, mediums in which shear waves dissipate quickly, such as water, air, and tissue, are assumed. The load is an electrical impedance connected to the terminals of the RX transducer.

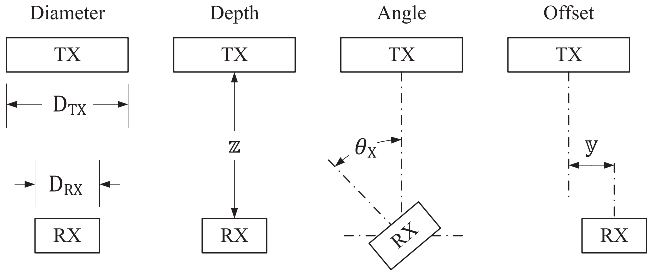

Figure 2. Definition of TX and RX diameters, depth, angle (orientation), offset (alignment).

The position of the RX relative to the TX can be defined by 3 parameters: depth, angle (orientation), and offset (alignment) as shown in figure 2. Depth, $\mathbb{z}$, is defined as the separation distance between the TX and RX along the propagation axis (z-axis). Angle, θ_X, is the x-axis rotation of the RX relative to the TX. Offset $\mathbb{y}$, is the y-axis displacement from the propagation axis. D_{TX} and D_{RX} are the diameters of the TX and RX respectively. It should be noted that this paper assumes transducers that have a circular cross-section and a flat face. The DOART modeling technique can be extended to any cross-sectional transducer shape by adding y-axis rotation and x-axis displacement degrees of freedom. DOART can also be extended to transducer faces with curvature by either developing an application specific version of the Reflected Grid Method (discussed later in this paper) or employing a more generalized ray tracing algorithm.

In DOART, the TX and RX transducers can be modeled by any equivalent circuit that (1) models an acoustic transducer, (2) has an electrical port and a mechanical or fluidic port, and (3) employs impedances with values that are independent of the impedances of other subsystems. For example, even though the Mason model and KLM model are equivalent to each other [17], the Mason model for a bulk-mode piezoelectric transducer (i.e. plate) could be used in the DOART system, but the KLM model could not because its front and back impedances are dependent on the impedances of the mediums and/or transducers attached to them. In this paper, an LC circuit model (shown in figure 3) that utilizes complex losses is employed as the TX and RX in order to compare experimental data to the DOART model.

The circuit parameters of the LC model are determined by first calculating the series resonance frequency, f_s in (1), based on the thickness, t_{pe}, and speed of sound, c_{pe}, of the piezo element. The parallel resonance frequency, f_p in (2), can then be calculated based on the series frequency where k_{33} is the 3-3 mode electromechanical coupling factor of the piezo element. The series inductance, L_s, is given in (3) where ρ_{pe} is the density and A_{pe} is area of the circular face of the

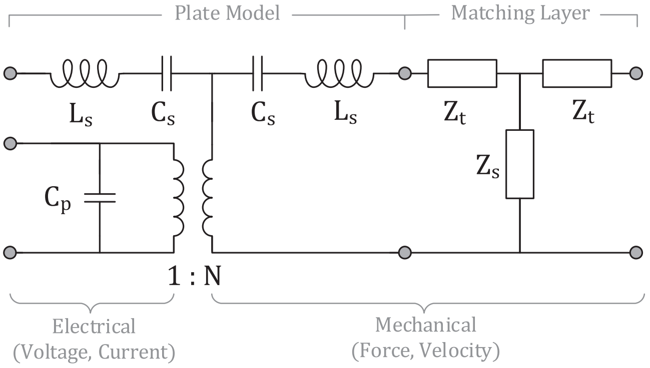

Figure 3. LC model for bulk-mode piezoelectric plate with circular cross-section. The model has one electrical port and two mechanical ports representing the terminals, and front and back of the piezo element respectively. An example matching layer is attached to the front mechanical port of the piezo.

piezo element. The series capacitance is calculated using the series inductance and series frequency in (4) where Q_{total} is the quality factor of the piezo element that may include effects such as resistance posed by the material's internal structure and viscous drag as the element vibrates in the medium. The parallel capacitance, C_p, is representative of the piezo element's electrical capacitance and is given in (5) where ϵ_{pe}^T is the permittivity at zero stress and $\tan\delta$ is the dielectric loss factor of the piezo element. Finally, the turns ratio, N, of the transformer, which allows the model an electrical and mechanical port, can be calculated from the other circuit parameters and is given in (6). Matching and backing layers can be added to the bulk-mode transducer model by placing a T-branch filter in series with either of the mechanical ports as shown in figure 3. The impedances Z_t and Z_s can be calculated from (7) and (8) respectively where ρ_{ml}, c_{ml}, A_{ml}, and t_{ml} are the density, speed of sound, circular face area, and thickness of the matching/backing layer respectively and f is the operating frequency.

$$f_s = \frac{c_{pe}}{2t_{pe}} \tag{1}$$

$$f_p = \left(\frac{4k_{33}^2 + \pi^2}{\pi^2}\right) f_s \tag{2}$$

$$L_s = 2\rho_{pe} A_{pe} t_{pe} \tag{3}$$

$$C_s = \frac{1}{4\pi f_s^2 L_s}\left(1 - \frac{j}{2Q_{total}}\right) \tag{4}$$

$$C_p = \frac{\epsilon_{pe}^T A_{pe}}{t_{pe}}(1 + j\tan\delta) \tag{5}$$

$$N = 2\pi f_p \sqrt{C_p L_s - \frac{4f_s^2 L_s C_p Q_{total}^2}{f_p^2(1+4Q_{total}^2)}} \tag{6}$$

$$Z_t = j\rho_{ml} c_{ml} A_{ml} \tan\left(\frac{\pi f t_{ml}}{c_{ml}}\right) \tag{7}$$

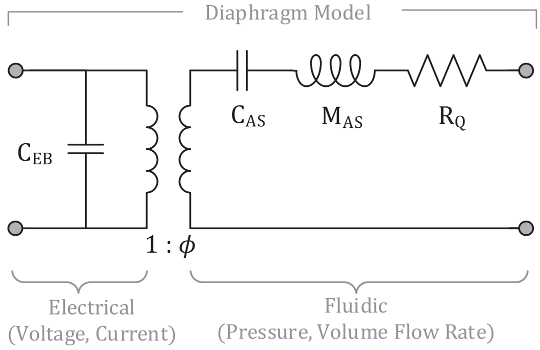

Figure 4. Network equivalent model of a piezoelectric flexure-mode transducer.

$$Z_s = -j\rho_{ml} c_{ml} A_{ml} \csc\left(\frac{2\pi f t_{ml}}{c_{ml}}\right) \tag{8}$$

Flexure mode transducers (i.e. diaphragms or PMUTS) are also supported in DOART by employing the network equivalent model developed in [18] and extended in [2] as shown in figure 4. The circuit parameters can be calculated for a partially covered diaphragm with a single piezo layer and a single elastic layer by referring to [18]. For an expanded version that accounts for an arbitrary number of elastic layers, refer to the working equations given in [19]. Note that in [19] there is a typo in equations 5, 8a–8c, 9, 10, 44, and 45 where the denominator should be $(1 - \nu^2)$ instead of $(1 - \nu)^2$. The notation in figure 4 is consistent with the notation in [18].

To calculate the average pressure radiating from the face of a TX bulk-mode transducer into the medium, a mechanical impedance can be attached to the front mechanical port of the transducer. The medium impedance from the Helmholtz integral, as described in [20, 21], is given in (9) where D is the diameter of the transducer of interest, H_1 is the first order Struve function, J_1 is the first order Bessel function, and k, ρ and c are the wave number, density, and speed of sound of the medium. The average pressure radiating from the TX face into the medium is then simply calculated as the force across the medium impedance divided by the transducer face area.

$$Z_{Medium} = \frac{\rho c \pi D^2}{4}\left(1 - \frac{2J_1(kD)}{kD} - \frac{2H_1(kD)}{kD} j\right) \tag{9}$$

The steps involved in calculating the power transferred to the load using the DOART modeling technique are illustrated in figure 5 and outlined in the following steps:

(1) Assemble the TX. The TX is assembled by attaching an electrical source to the electrical port, matching and backing layers to the mechanical/fluidic port(s) (optional), and an infinite medium to the mechanical/fluidic port(s). In the case of the piezoelectric plate transducer, the back mechanical port is terminated with a short to approximate the back medium as being either air or a vacuum.

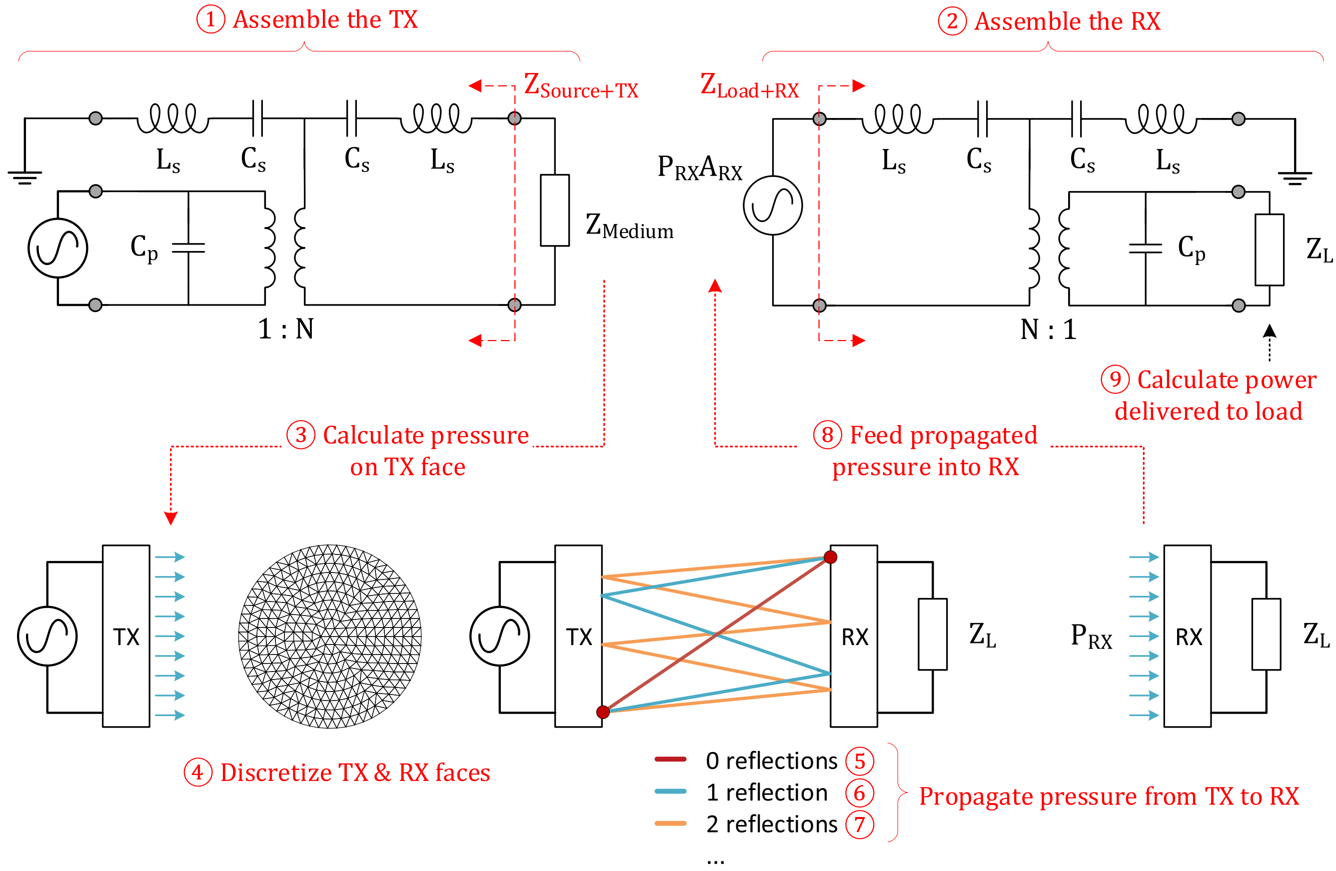

Figure 5. Diagram of the steps involved in calculating the power transferred to the load using the DOART modeling technique.

(2) Assemble the RX. The RX is assembled by attaching an electrical load to the electrical port, matching and backing layers to the mechanical/fluidic port(s) (optional), and a mechanical/fluidic source to the front mechanical/fluidic port. The source represents the average pressure on the RX face as calculated in steps 6 to 8.

(3) Calculate pressure on TX face. Pressure on the TX face, before propagation, is found using the assembled TX circuit model in an infinite medium. In the case of the plate TX, the force across the infinite medium circuit element, Z_{Medium}, is calculated in response to the source excitation. This force is divided by the TX area to obtain the average pressure on the TX face.

(4) Discretize TX and RX faces. The TX and RX faces are discretized into 2D elements. This paper uses Delaunay triangulation to create triangular elements.

(5) Propagate pressure from TX to RX. The pressure emitted from each element on the TX face is propagated to each element on the RX face using a modified version of Huygens principle as discussed in the Modified Huygens Principle section of this paper.

(6) Propagate pressure for 1 reflection (TX to RX to TX to RX). The Reflected Grid Method is used to determine the direction that each pressure ray emitted from each TX element should be propagated in order to reach the center of each RX element after 1 reflection. Each pressure ray is propagated using the modified version of Huygens principle and reflected using principles of ray tracing as discussed in the Reflected Grid Method section of this paper.

(7) Repeat step 6 for 2, 3, 4, … etc reflections.

(8) Feed propagated pressure into RX model. The pressure contribution from each reflection is summed for each RX element. The summed pressure for each RX element on the RX face is then averaged and fed into the RX circuit as a pressure source. In the case of the plate transducer, the pressure is multiplied by the RX area to give a force before being fed into the RX circuit.

(9) Calculate power delivered to the load.

Modified Huygens principle

To calculate the pressure transmitted from the TX face to the RX face, an expanded version of Huygens principle is used. Huygens principle can be summarized as follows: (1) The TX and RX faces are discretized into smaller elements. Each of these elements is treated as a half-spherically radiating pressure source. In DOART, the elements are triangular and can be obtained by applying Delaunay triangulation to uniformly spaced points around uniformly spaced concentric circles as shown in figure 6. This discretization method is used to minimize element area variation while maintaining the ability to properly represent the circular shape of the transducer face

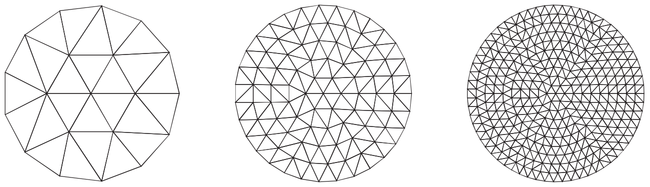

Figure 6. Discretization method of TX and RX faces using Delaunay triangulation for 2, 5, and 10 concentric circles with even spacing.

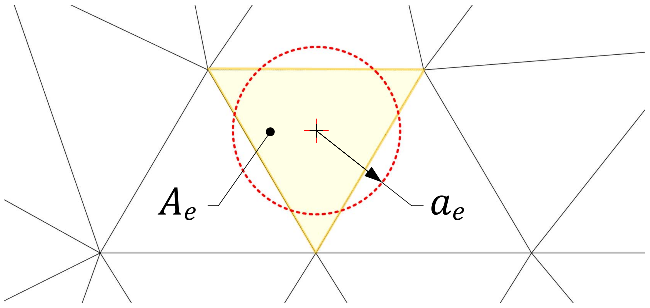

Figure 7. A single triangular element is treated as a circular piston with the same area when calculating pressure radiating from the TX face.

when using larger elements. For example, 10 concentric circles result in 629 elements with a standard deviation of 2.59% variation in element area. (2) The pressure from a single TX element to a single RX element is calculated in the frequency domain. Each triangular element is approximated as a circular piston of equal area, A_e, and radius, a_e (see figure 7), when calculating the element-to-element pressure. The differential pressure calculation, given in (10), takes into account magnitude, phase, divergence, absorption, and directionality where f is the frequency of the pressure source, d is the distance between the TX and RX element, $P_{e,TX}$ and $P_{e,RX,0}$ are the pressure at the TX and RX elements respectively, k is the wave number, α_0 is the absorption coefficient, n is the absorption exponent, f_{MHz} is the frequency in MHz, and ϕ is the angle of the pressure ray relative to the propagation axis. It should be noted that the directionality component can be neglected for improved computational efficiency without incurring significant error. This error is most noticeable for significant offset values, high frequencies, large TX elements, and shallow depth values. (3) The pressure contribution from each element on the TX to a single element on the RX is summed. The resulting complex pressure is the contribution of the entire TX on that single RX element if there are no pressure reflections between the TX and RX. (4) The complex pressure contribution of the TX on each RX element is calculated. (5) The effective pressure on the RX face, for zero reflections, is calculated as the average complex pressure of all the RX elements. It should be noted that results reported in the Experimental Setup & Validation section of this paper are load voltages reported as the magnitude of the complex result.

$$P_{e,RX,0} = P_{e,TX} \frac{A_e J_1(ka_e \sin(\phi))}{\pi d a_e \sin(\phi)} e^{-d\alpha_0 f_{MHz}^n + \left(-kd+\frac{\pi}{2}\right)j} \quad (10)$$

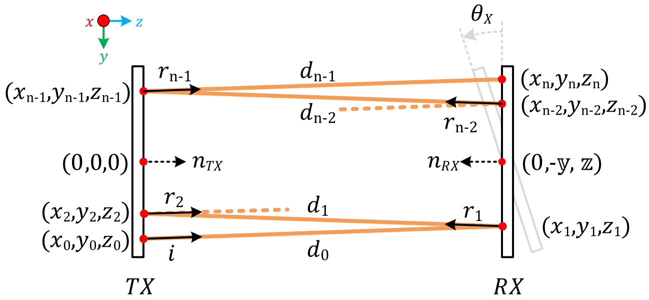

Figure 8. Diagram of ray tracing concept, variables, relative TX and RX geometry and Cartesian coordinate system orientation.

Reflected Grid method

Using the modified version of Huygens principle to calculate the pressure propagating from the TX to the RX for zero reflections is only the first step to properly modeling the entire DOART system. The next step is to account for the pressure reflections back and forth between the TX and RX. To accomplish this computation efficiently while still being able to use Huygens principle, ray tracing can be employed with the following assumptions: (1) The TX and RX transducer faces are flat (i.e. all points of the transducer face lie in a plane). (2) The RX can only move in 3 degrees of freedom with respect to the TX. These degrees of freedom are defined as depth, offset (alignment), and angle (orientation) in figure 2. (3) The medium between the TX and RX is a single homogeneous material. It should be noted that tissue is not a homogeneous material, but the attenuation of acoustic power traveling through tissue can be approximated by treating tissue as a homogeneous material with an appropriate absorption coefficient. This approximation is commonly used for general modeling of acoustic power transfer systems where specific tissue inhomogeneities are not specified. (4) The TX is fixed in the coordinate system and the center point of its face is the origin. This means that only the RX experiences a shift in depth, offset, and angle within the defined coordinate system.

To ensure that the pressure contribution of a specific single TX element on a specific single RX element can be calculated for any number of reflections, analytical relationships in the form of series solutions for any number of reflections are derived for intersection points on the RX and TX faces, (x_n, y_n, z_n), distances between intersection points, d_n, and the direction of reflected pressure rays, r_n, which is written as $\langle x_{r_n}, y_{r_n}, z_{r_n} \rangle$ in vector form. For clarification, zero reflections is defined as a pressure ray traveling from the TX to the RX (i.e. TX $\rightarrow$ RX). One reflection is defined as TX $\rightarrow$ RX $\rightarrow$ TX $\rightarrow$ RX, two reflections is then TX $\rightarrow$ RX $\rightarrow$ TX $\rightarrow$ RX $\rightarrow$ TX $\rightarrow$ RX, etc. A diagram of the ray tracing problem in Cartesian coordinates is given in figure 8 where n_{TX} and n_{RX} are the normal vectors to the TX and RX faces respectively.

Utilizing principles of ray tracing, treating the TX and RX faces as infinite planes, and defining the constants (11)(12)(13)(14), a compact series solution for the remaining variables in the ray tracing diagram for an arbitrary number of reflections can be derived. (15)(16)(17)(18) give the x, y, and z coordinates of the points where the pressure ray intersects the TX and RX planes. Even subscripts represent points on the TX and odd subscripts represent points on the RX. Note that these points are where the pressure ray intersects the plane of the transducer face, not necessarily the transducer. In implementation, each ray must be checked to determine if it has strayed or hit the transducer face. (19)(20) give the distances between subsequent intersection points. For example, d_0 is the distance between point 0 and 1, and d_1 is the distance between point 1 and 2. (21)(22) give the directions of the reflected vector at each intersection point. Note that r_0 is equal to the initial vector i.

$$\mathscr{A} = -\mathbb{y}\sin(\theta_X) - \mathbb{z}\cos(\theta_X) \tag{11}$$

$$\mathscr{S} = (1 - 2\sin^2(\theta_X)) \tag{12}$$

$$\mathscr{C} = (1 - 2\cos^2(\theta_X)) \tag{13}$$

$$\mathscr{T} = \sin(2\theta_X) \tag{14}$$

$$x_n = x_0 + x_i\left(\sum_{k=0,1,2,3\ldots}^{n-1} d_k\right) \tag{15}$$

$$y_n = y_0 + \sum_{k=0}^{n-1} d_k y_{r_k} \tag{16}$$

$$z_n = 0 \rightarrow n = 0, 2, 4, 6,\ldots \text{ even} \tag{17}$$

$$z_n = d_{n-1} z_{r_{n-1}} \rightarrow n = 1, 3, 5, 7,\ldots \text{ odd} \tag{18}$$

$$d_n = \left(\frac{\mathscr{A} - \sin(\theta_X)\, y_n}{\sin(\theta_X)\, y_{r_n} - \cos(\theta_X)\, z_{r_n}}\right) \rightarrow n = 0, 2, 4, 6,\ldots \text{ even} \tag{19}$$

$$d_n = -\frac{z_n}{z_{r_n}} \rightarrow n = 1, 3, 5, 7,\ldots \text{ odd} \tag{20}$$

$$\vec{r}_n = (x_i,\ y_{r_{n-1}}\mathscr{S} + z_{r_{n-1}}\mathscr{T},\ z_{r_{n-1}}\mathscr{C} + y_{r_{n-1}}\mathscr{T}) \rightarrow n = 1, 3, 5, 7,\ldots \text{ odd} \tag{21}$$

$$\vec{r}_n = (x_i,\ y_{r_{n-1}},\ -z_{r_{n-1}}) \rightarrow n = 2, 4, 6, 8\ldots \text{ even} \tag{22}$$

The initial vector I is not solved for in the equations mentioned above. i represents the direction that the pressure ray must be projected from a specified point on the TX in order to reach a specified point on the RX after n_r reflections. Solving for i for a known starting point on the TX and ending point on the RX is essential to calculating the correct distances, reflection directions, and reflection coefficients. For the case that $\theta_X = 0$, a solution to i, (23), can be obtained by inspection where n_r is the number of reflections (note that $n = 2n_r + 1$). However, to derive an analytical solution for i when $\theta_X \neq 0$ is not trivial. To overcome this obstacle, the secant method for root finding can be used to find the roots to the spatial error between the center of the targeted RX element and where the trajectory of a guessed initial vector actually hits. In this implementation, the error in the X and Y components of the initial vector are separately and simultaneously minimized. This method, in practice using MATLAB, converges in less than 10 iterations and can be efficiently applied to a matrix of initial vectors that represent pressure contributions from every element on the TX to every element on the RX.

$$\vec{i} = \left\| \left(\frac{x_{2n_r+1} - x_0}{2n_r + 1},\ \frac{y_{2n_r+1} - y_0}{2n_r + 1},\ z_{2n_r+1} - z_0\right)_2 \right\| \tag{23}$$

$$P_{e,RX,n_r} = P_{e,TX}\frac{A_e J_1(ka_e\sin(\phi))}{\pi\left(\sum_{m=0}^{2n_r} d_m\right) a_e\sin(\phi)}\cdots \times e^{-\left(\sum_{2n_r}^{m=0} d_m\right)\alpha_0 f_{MHz}^n + \left(-k\left(\sum_{m=0}^{2n_r} d_m\right) + \frac{\pi}{2}\right) j}\cdots \times \left(\prod_{m=1}^{n_r} R_{2m-1}R_{2m}\right) \tag{24}$$

After solving for the initial vector, the complex pressure contribution from a single TX element on a single RX element for an arbitrary number of reflections (greater than zero) can be calculated by modifying (10) to include reflection coefficients at the TX and RX faces. This expanded version is given in (24) where R_n is the reflection coefficient at point n (odd n is at the RX face and even n is at the TX face) as defined in the diagram in figure 8. The reflection coefficient is given in (25) and (26) where $Z_{Source+TX}$ is the acoustic impedance of the source and TX (the TX includes the piezo element with any matching and backing layers attached) as seen by the medium, $Z_{Load+RX}$ is the acoustic impedance of the load and RX as seen by the medium, $\theta_{t,n}$ is the transmitted angle of the pressure ray into the transducer, $\theta_{i,n}$ is the incident angle of the pressure ray onto the transducer face, and ρ and c are the density and speed of sound of the medium respectively. The cosine of the incident angle is given in (27) and (28) for the cases that the pressure ray intersects the RX and TX planes respectively. The cosine of the transmitted angle is given in (29) and (30) for the cases where the pressure ray intersects the RX and TX planes respectively where c_{RX} and c_{TX} are the speed of sound of the material of the RX and TX that is in contact with the medium respectively. It should be noted that the reflection coefficients are affected by any electrical impedances and matching layers attached to the TX and RX transducers.

$$R_n = \frac{\dfrac{Z_{Load+RX}}{\cos(\theta_{t,n})} - \dfrac{\rho c}{\cos(\theta_{i,n})}}{\dfrac{Z_{Load+RX}}{\cos(\theta_{t,n})} + \dfrac{\rho c}{\cos(\theta_{i,n})}} \rightarrow n = 1, 3, 5, 7,\ldots \text{ odd} \tag{25}$$

$$R_n = \frac{\dfrac{Z_{Source+TX}}{\cos(\theta_{t,n})} - \dfrac{\rho c}{\cos(\theta_{i,n})}}{\dfrac{Z_{Source+TX}}{\cos(\theta_{t,n})} + \dfrac{\rho c}{\cos(\theta_{i,n})}} \rightarrow n = 2, 4, 6,\ldots \text{ even} \tag{26}$$

$$\cos(\theta_{i,n}) = -\vec{r}_n \cdot \vec{n}_{RX} \rightarrow n = 1, 3, 5, 7,\ldots \text{ odd} \tag{27}$$

$$\cos(\theta_{i,n}) = -\vec{r}_n \cdot \vec{n}_{TX} \rightarrow n = 2, 4, 6, 8,\ldots \text{ even} \tag{28}$$

$$\cos(\theta_{t,n}) = \sqrt{1 - \left(\frac{c_{RX}}{c}\right)\cos^2(\theta_{i,n})} \rightarrow n = 1, 3, 5, 7,\ldots \text{ odd} \tag{29}$$

$$\cos(\theta_{t,n}) = \sqrt{1 - \left(\frac{c_{TX}}{c}\right)\cos^2(\theta_{i,n})} \rightarrow n = 2, 4, 6, 8,\ldots \text{ even} \tag{30}$$

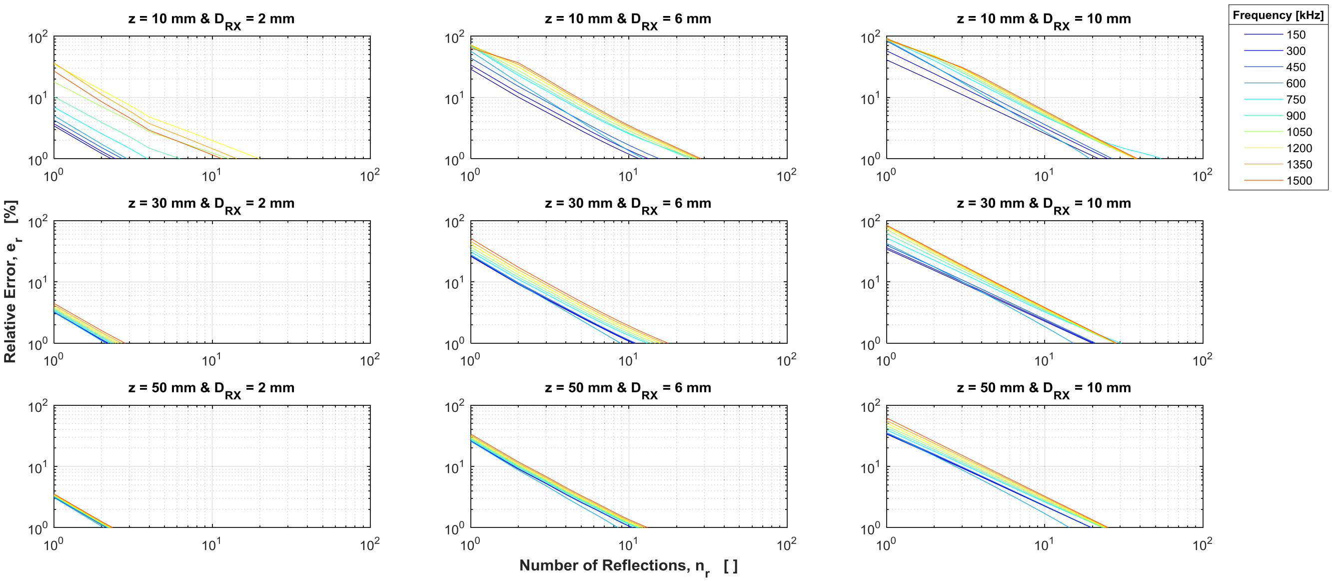

Figure 9. Relative error of average RX pressure calculation for a 10 mm diameter TX as a function of number of reflections for various frequencies (blue = 150 kHz, red = 1500 kHz). Each plot represents a different depth (z) and RX diameter (d_{RX}). The data was simulated using 5 concentric discretizing circles (157 elements) for both the TX and RX.

The pressure on a single element on the RX face is then calculated as the summation of the pressure contributions from all TX elements summed over an infinite number of reflections as given in (31). Once the pressure for all RX elements is calculated, the pressure on the RX face, as seen by the load, is calculated as the average pressure of all RX elements as given in (32) where N_{RX} is the number of elements on the RX face. In practice, calculating an infinite number of reflections is not possible because the computation time for each subsequent reflection gets exponentially longer. However, a good approximation can be achieved for a relatively cheap computation time (compared to finite element methods) by wisely choosing the number of elements and reflections to use. The average pressure over all RX elements, PRX, is used as the input pressure source for the RX circuit. The resulting power delivered to the load can then be calculated.

$$P_{e,RX} = \sum_{n_r=0}^{\infty} P_{e,RX,n_r} \tag{31}$$

$$P_{RX} = \frac{1}{N_{RX}} \sum_{k=0}^{N_{RX}} P_{e_k\,,\,RX} \tag{32}$$

Convergence and timing

The relative error in the RX pressure calculation between each subsequent reflection, as defined in (33), converges to zero as the number of reflections used goes to infinity. The rate of convergence is dependent on operating frequency, diameter, depth, and the material properties of the medium. As an example, the relative error as a function of reflections for a 10 mm-diameter TX operating in water at 150 kHz to 1500 kHz in increments of 150 kHz as RX diameter and depth are varied is shown in figure 9. In the data presented, more reflections are required to achieve smaller relative errors for higher frequencies, larger RX diameters, and shallower depths. The cases shown are for an RX with offset, y, and angle, θ_X, equal to zero. In cases where the RX has an offset or angle not equal to zero, significantly fewer pressure rays are able to reflect between the TX and RX. For large values of offset or angle, reflections between TX and RX are not possible. Consequently, the relative error converges much faster for misaligned and/or misoriented transducers meaning that significantly fewer reflections are required for effective convergence.

$$e_r = \frac{1}{N_{RX}} \sum_{m=1}^{N_{RX}} \frac{P_{e_m,RX,(n_r+1)}}{\sum_{k=0}^{n_r} P_{e_m,RX,k}} = \frac{P_{RX,(n_r+1)} - P_{RX,n_r}}{P_{RX,n_r}} \tag{33}$$

To further illustrate the effect of subsequent reflections on relative error, pressure as a function of depth for a 10-mm-diameter TX and RX operating at 750 kHz for various number of reflections is given in figure 10. The figure shows that each additional reflection more faithfully reproduces the pressure profile. It should be noted that high Q TX transducers and low-loss mediums require a higher number of reflections to resolve the sharp pressure peaks on the RX face than low Q TX transducers and lossy mediums that produce flatter pressure profiles on the RX face.

In addition to considering the relative error in terms of reflections, the number of elements chosen to discretize the TX and RX faces must be considered. The number of elements on a circular transducer face is a function of the number of discretizing circles chosen as explained in the Modified Huygens Principle section of this paper and given in table 1. The relative error as a function of discretizing circles for a 10 mm-diameter TX operating in water at 150 kHz to 1500 kHz in increments of 150 kHz as RX diameter and depth are varied is given in figure 11. It is notable that the relative

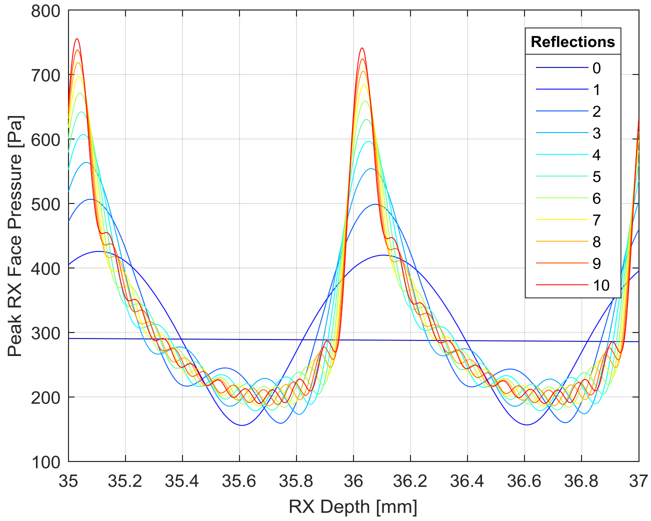

Figure 10. RX face pressure as a function of depth for various reflections. TX and RX are simulated using 5 discretizing circles (157 elements) each. Each additional reflection better resolves the sharp pressure peaks.

Table 1. Number of elements as a function of number of circles.

Circles	Elements	Circles	Elements	Circles	Elements
0	1	7	308	14	1232
1	6	8	402	15	1414
2	25	9	509	16	1609
3	57	10	629	17	1817
4	101	11	761	18	2037
5	157	12	905	19	2269
6	226	13	1062	20	2514

error behaves differently as a function of elements compared to reflections. In the reflections case, more reflections were required to reduce the relative error for larger RX diameters. In the elements case, the relative error converges faster when the TX and RX have the same diameter. This occurs because the effective number of elements is fewer in the region of highest reflection activity when the TX and RX have different diameters as shown in figure 12. In the case of the figure, the number of element used for the TX (case on the right side) would need to be increased to reduce the relative error. Best practice is to match the radial spacing of the TX and RX elements as closely as possible and ensure that both radial spacings are less than or equal to half of the wavelength in the medium.

The simulation time is a function of the number of reflections and elements used. A sample of simulation times per data point as a function of number of reflections and circles is given in figure 13. Simulation times were measured using an Asus K501UX that has an i7-6500U (2.5 GHz) processor and 12 GB RAM. The simulation times can be further reduced by implementing a ray straying programmatic condition. The condition ceases further simulation of subsequent reflections when all pressure rays have strayed. This condition results in significant time savings when simulating cases where angle and offset are not equal to zero.

To compare DOART and finite element simulation time, the known time for an axis-symmetric finite element simulation was compared to a DOART simulation crafted to match the finite element simulation scenario as closely as possible. The DOART simulations were run using the Asus K501UX specified above, while the finite element simulations were run on a virtual machine with a dual-core AMD Opteron 8220 (2.79 GHz) processor with 32 GB RAM. In both cases, a 50 mm TX and 12.7 mm RX in water at 50 mm depth, 0 mm offset, and 0° angle were used. The COMSOL finite element simulation used 378 elements for the TX, 112 elements for the RX, and 119352 elements for the medium. The DOART simulation used 2514 elements (20 circles) for the TX and 157 elements (5 circles) for the RX. Both cases use 2 wavelengths in the radial direction and 10 wavelengths in the propagation direction. The finite element simulation took 73 s per data point (a data point is where all parameters have a single value) while the DOART simulation took 11 s at 10 reflections (2.85% relative error), 40 s at 20 reflections (0.49% relative error), and 868 s at 100 reflections (0.000037% relative error). In cases where offset and angle are zero, an axis-symmetric finite element simulation can be used and the time per data point will be on the same order as DOART. As frequency increases, both the finite element and DOART simulation times increase because the wavelength gets smaller. As depth increases, the finite element simulation time increases because more elements are required to model the extra length of medium, but DOART simulation time decreases because pressure rays stray quicker and thus fewer reflections are required. When working with finite element simulations for cases where offset and angle are not equal to zero, 3D elements are required and, consequently, the simulation time dramatically increases. A COMSOL simulation of the same system using 3D elements (337380 elements for the TX, 26192 elements for the RX, and 5760776 elements for the medium) took 2777 s to simulate per data point, more than an order of magnitude greater than DOART. DOART time savings become significant in this case because DOART simulation time decreases for cases where offset and angle are not equal to zero. This is due to the ray straying programmatic condition discussed previously. For cases where angle is not equal to zero and reflections do not stray quickly (shallow angles), the simulation time can increase as a function of the number of reflections used. This is due to the extra computation involved in using the secant method to find the initial vector for the Reflected Grid Method as described previously.

Experimental setup and validation

To test the abilities and limitations of the DOART modeling technique, simulation data is compared to experimental data. Piezoelectric transducers, in a water-filled acoustic test tank equipped with a positioning apparatus, were used to obtain the experimental data. The test tank is a 59 × 28 × 28 cm acrylic tank lined with ultra-soft polyurethane acoustic absorbers

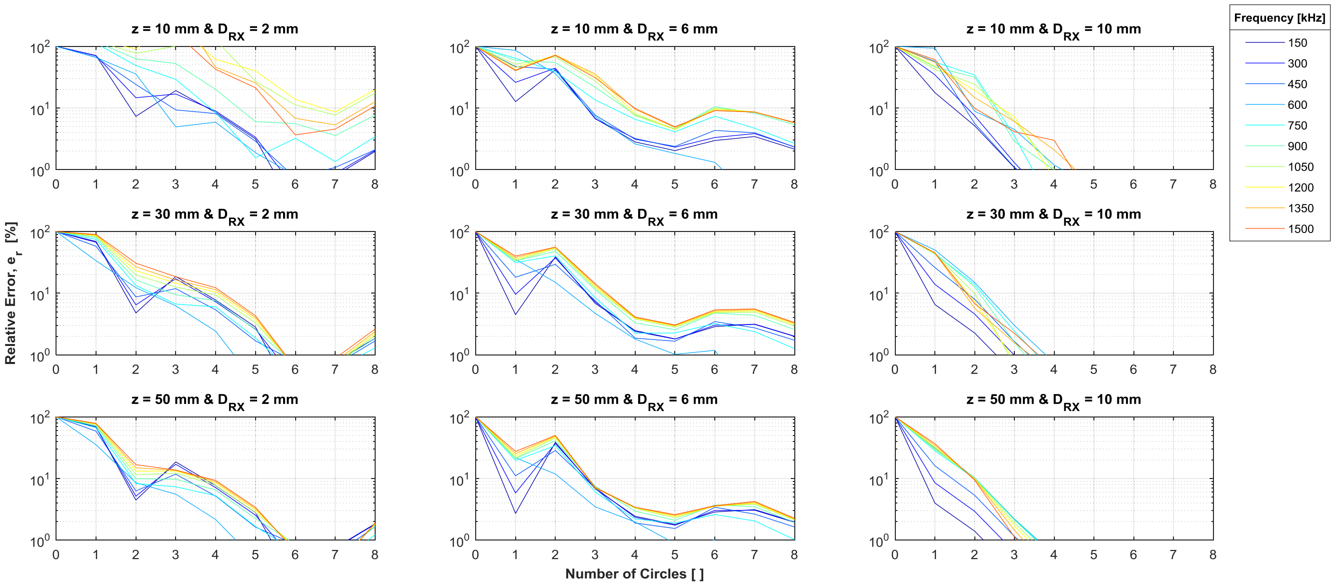

Figure 11. Relative error of average RX pressure calculation for a 10 mm diameter TX as a function of TX and RX discretizing circles for various frequencies (blue = 150 kHz, red = 1500 kHz). Each plot represents a different depth (z) and RX diameter (d_{RX}). The data was simulated using 100 reflections.

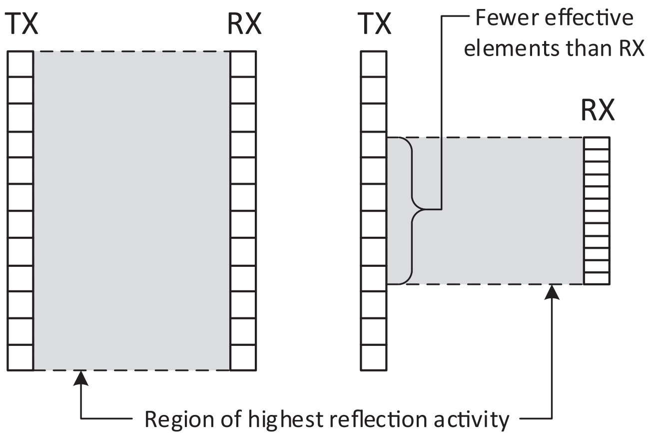

Figure 12. Definition of region of highest reflection activity (gray shaded area). The TX and RX in both cases have the same number of elements, but the TX on the right has fewer effective elements in the region of highest reflection activity. Mismatched element spacing in the radial direction can increase error.

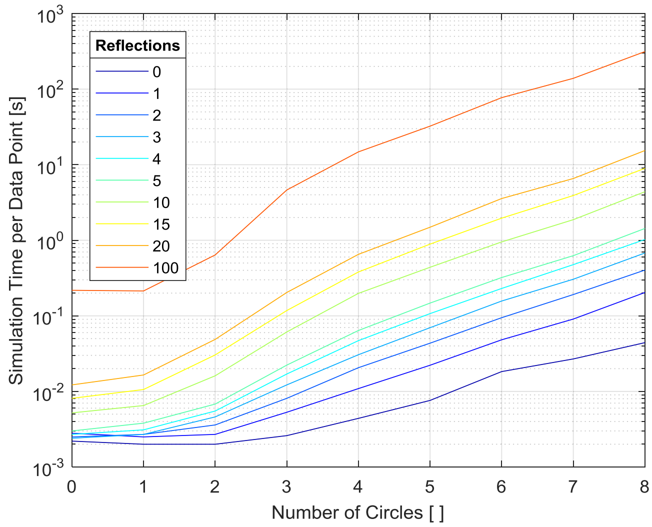

Figure 13. Simulation time per data point as a function of number of discretizing circles on the TX and RX for various number of reflections. Simulation time represents maximum expected simulation time where angle and offset are zero.

(McMaster Carr, 8514K75). The absorbers are 12.7 mm thick and experimentally exhibit an average of 90.6% pressure attenuation after one pass on a pulse-echo test between the frequencies of 5 kHz and 1.25 MHz [2]. The transducers used in the experiment will be referred to by their serial numbers: PL3, PA2, PB4, and PB6. Material properties for the transducers are given in table 2. PL3 is a bulk-mode piezo element that is press fit into a PVC housing and sealed against water on the back side. The piezo element is 50 mm in diameter, 3 mm thick, and has wrap-around electrodes. PA2 is a bulk-mode piezo element that is set atop an ABS tube with cyanoacrylate and sealed against water on the back side. The piezo element is 12.7 mm in diameter, 3.43 mm thick, and has a standard separate electrode on each face. PB4 and PB6 are bulk-mode piezo elements that are press fit into an ABS housing and sealed against water on the back side. The piezo element is 12.7 mm in diameter, 1.9 mm

Table 2. Piezoelectric element properties of experimental transducers.

	Var	Units	PL3	PA2	PB4/6
Diameter	d_{pe}	mm	50	12.7	12.7
Piezo Thickness	t_{pe}	mm	3.00	3.43	1.90
Density	ρ_{pe}	kg m^{-3}	7900	7600	7600
Speed of Sound	c_{pe}	m s^{-1}	3955	4310	4025
Coupling Coeff.	k_{33}	—	0.65	0.45	0.46
Rel. Permittivity	ϵ_{pe}	—	1400	1900	1950
Mechanical Q	Q_m	—	1800	80	80
Dielectric Loss	tan δ	%	0.4	2	1.5

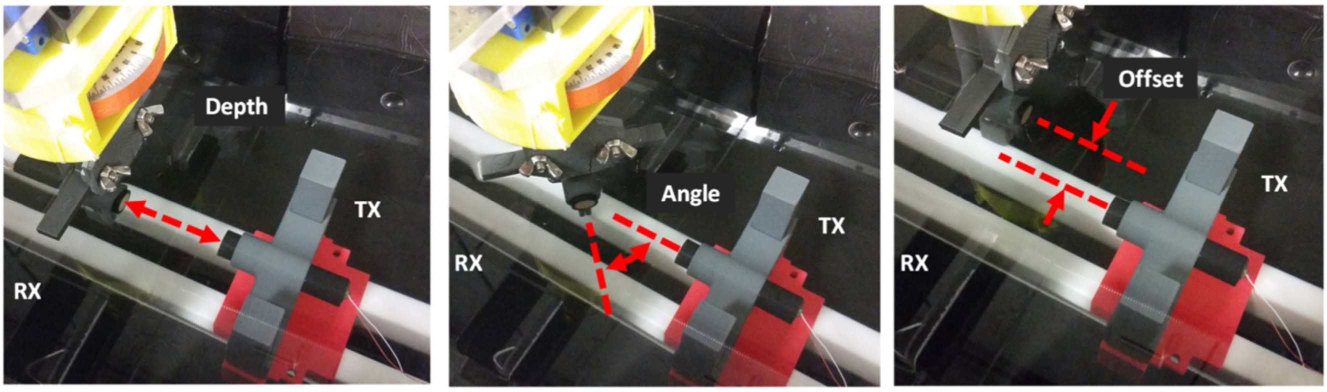

Figure 14. Test setup showing PB4 (TX) and PB6 (RX) in an acoustic test tank filled with distilled water and lined with acoustic absorbers. Depth, angle, and offset measurement are demonstrated.

thick, and has wrap-around electrodes. The TX transducer is powered by a Rigol DG1022A function generator connected to a Rigol PA1011 power amplifier. The RX has a resistive load connected across its terminals. RMS voltage measurements across the RX load were recorded using a PicoScope 2206.

In this paper, residuals are used to quantitatively compare the variation between experiment and simulation data in terms of magnitude and shape. The magnitude variation is defined as the average of experimental minus simulated RX load voltage divided by the maximum simulated RX load voltage. The shape variation is defined as the average of the magnitude of the difference between the normalized experimental and normalized simulated RX load voltages and is expressed as a percentage. The idea behind the shape variation is to match the simulated and experimental magnitudes as much as possible and then find the variation between them.

PB4 and PB6 were placed in the acoustic test tank as shown in figure 14. RX load voltage was recorded as a function of depth, angle, and offset for a resistive RX load of 986 Ω, a voltage source impedance of 2 Ω, and source voltage of 16 V at 1058824 Hz. Depth measurements were taken from 12.5 to 16 mm in increments of 0.1 mm at 0° angle and 0 mm offset and are given in figure 15. The depth magnitude variation is 2.1% and the shape variation is 4.5%. Angle measurements were taken from −45° to 45° in increments of 1° at 51 mm depth and 0 mm offset and are given in figure 16. The angle magnitude variation is 3.4% and the shape variation is 3.8%. Offset measurements were taken from −30 mm to 30 mm in increments of 1 mm at 51 mm depth and 0° angle and are given in figure 17. The offset magnitude variation is 0.2% and the shape variation is 3.1%. Simulation data were obtained using 5 circles for both PB4 and PB6 with 4 reflections. The simulation time was 0.0974 s per depth data point, 0.149 s per angle data point, and 0.0496 s per offset data point.

PL3 and PA2 were then placed in the acoustic test tank and RX load voltage was recorded as a function of offset separately at a peak and at a valley near 50 mm depth at 0° angle. The RX had a resistive load of 100 Ω with a source impedance of 2 Ω and source voltage of 6.79 V at 642 kHz. Offset measurements were taken from −50 mm to 50 mm in

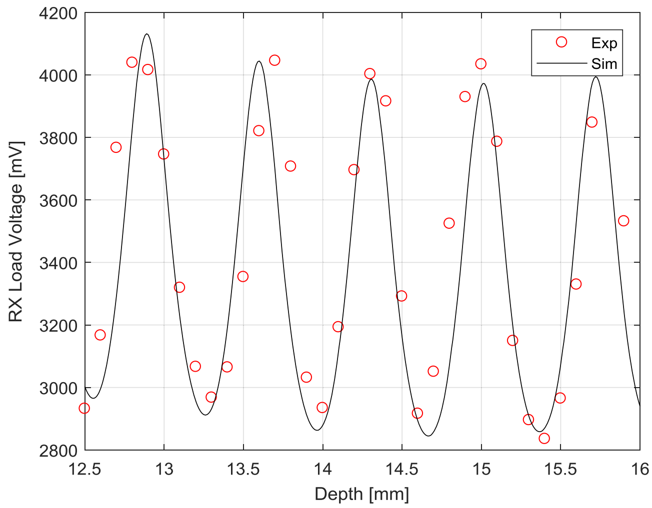

Figure 15. RX load voltage as a function of depth at 1058824 Hz at 0° angle and 0 mm offset for PB4 (TX) and PB6 (RX).

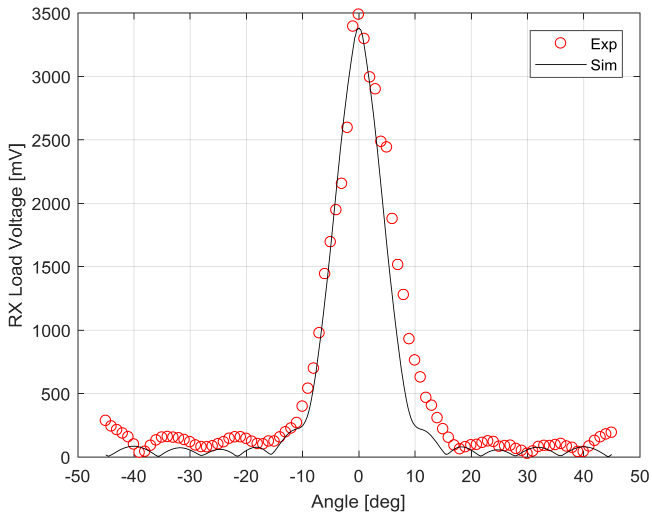

Figure 16. RX load voltage as a function of angle at 1058824 Hz at 51 mm depth and 0 mm offset for PB4 (TX) and PB6 (RX).

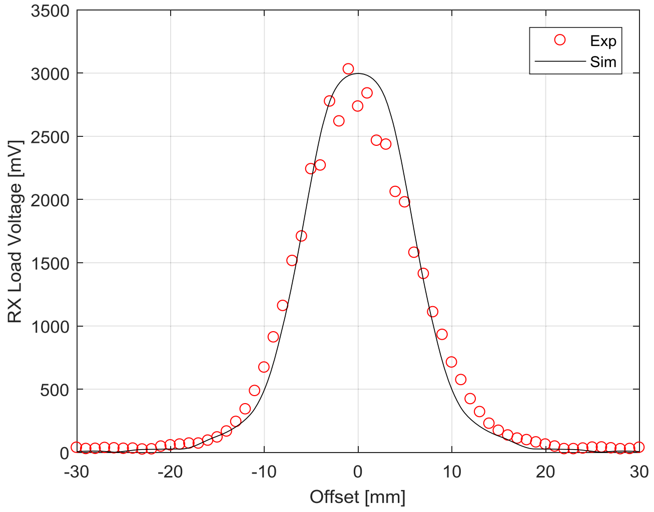

Figure 17. RX load voltage as a function of offset at 1058824 Hz at 51 mm depth and 0° angle for PB4 (TX) and PB6 (RX).

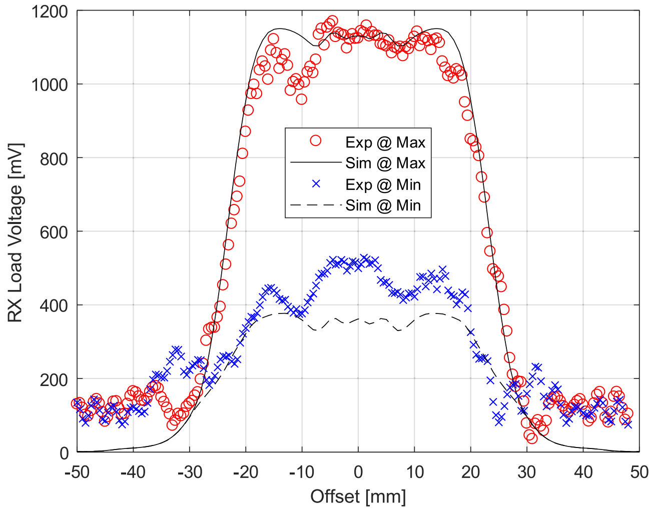

Figure 18. RX load voltage as a function of offset at 624 kHz for PL3 (TX) and PA2 (RX). Offset profiles are taken at a peak and valley around 50 mm depth at 0° angle.

increments of 0.5 mm and are given in figure 18. The offset magnitude variation is 1.5% for the peak and 23% for the valley. The shape variation is 6.6% for the peak and 16.5% for the valley. Simulation data were obtained using 15 circles for PL3 (TX), 6 circles for PA2 (RX), and 8 reflections. Simulation time per data point was 3.86 s. All simulation data assumes a depth and frequency tolerance of less than 0.35%.

Variance could be attributed to the precision and manual operation of the positioning apparatus, wrap around electrodes that cause dead spots in the piezo elements, and the one-dimensional circuit model used to model the transducers. There is no doubt that finite-element simulations have greater capabilities in handling more of the details such as non-homogeneous media, dead spots in transducers, all modes of the transducers, etc. However, considering the quick simulation times and achievable variance demonstrated in this paper, DOART can be an extremely useful tool for exploring parameter sweeps and quickly designing acoustic power transfer systems in a better-than-first-order fashion.

Conclusion

This paper presented the DOART modeling technique. The DOART system consists of 5 subsystems: source, TX, medium, RX, and load. A modified version of Huygens principle and the Reflected Grid Method were presented as a means of modeling beam spreading and TX and RX transducers of differing diameters in 3D space with 3 degrees of freedom. Experimental work was presented and compared with DOART simulations in terms of magnitude and shape of the received voltage signal. The quicker-than-finite-element simulation times, 3D modeling capabilities, and variances that can be considered reasonable for a number of applications make DOART a useful tool for acoustic power transfer system design and parameters sweeps.

Funding

The authors gratefully acknowledge funding from the National Science Foundation under grant number ECCS-1408265.

ORCID iDs

David B Christensen https://orcid.org/0000-0003-1488-1534

References

[1] Basaeri H, Christensen D B and Roundy S 2016 A review of acoustic power transfer for bio-medical implants *Smart Mater. Struct.* **2** 1–23
[2] Christensen D B and Roundy S 2015 Ultrasonically powered piezoelectric generators for bio-implantable sensors: plate versus diaphragm *J. Intell. Mater. Syst. Struct.* **27** 1092–105
[3] Song S H, Kim A and Ziaie B 2015 Omni-directional ultrasonic powering for mm-scale implantable biomedical devices *Biomed. Eng. IEEE Trans.* **62** 2717–23
[4] Hori Y, Fujimori K, Tsuruta K and Nogi S 2012 Design and development of highly efficient transducer for ultrasonic wireless power transmission system *IEEJ Trans. Electron. Inf. Syst.* **132** 337–43
[5] Ozeri S and Shmilovitz D 2014 Simultaneous backward data transmission and power harvesting in an ultrasonic transcutaneous energy transfer link employing acoustically dependent electric impedance modulation *Ultrasonics* **54** 1929–37
[6] Chou T C, Subramanian R, Park J and Mercier P P 2014 A miniaturized ultrasonic power delivery system *IEEE 2014 Biomed. Circuits Syst. Conf. BioCAS 2014—Proc.* pp 440–43
[7] Charthad J, Weber M J, Chang T C and Arbabian A 2015 A mm-sized implantable medical device (IMD) with ultrasonic power transfer and a hybrid bi-directional data link *IEEE J. Solid-State Circuits* **50** 1741–53
[8] Ozeri S and Shmilovitz D 2010 Ultrasonic transcutaneous energy transfer for powering implanted devices *Ultrasonics* **50** 556–66

[9] Shigeta Y, Hori Y, Fujimori K, Tsuruta K and Nogi S 2011 Development of highly efficient transducer for wireless power transmission system by ultrasonic *2011 IEEE MTT-S Int. Microwave Workshop Series on Innovative Wireless Power Transmission: Technologies, Systems, and Applications* pp 171–74

[10] Denisov A and Yeatman E 2010 Ultrasonic versus inductive power delivery for miniature biomedical implants *Body Sensor Networks BSN 2010 Int. Conf. on* no. June pp 84–9

[11] Ozeri S, Spivak B and Shmilovitz D 2012 Non-invasive sensing of the electrical energy harvested by medical implants powered by an ultrasonic transcutaneous energy transfer link *IEEE Int. Symp. Ind. Electron.* pp 1153–7

[12] Mo C, Hudson S and Radziemski L J 2013 Effect of misalignment between ultrasound piezoelectric transducers on transcutaneous energy transfer *Proc. SPIE* **8688** 868814

[13] Shahab S and Erturk A 2014 Contactless ultrasonic energy transfer for wireless systems: acoustic-piezoelectric structure interaction modeling and performance enhancement *Smart Mater. Struct.* **23** 125032

[14] He Q, Liu J, Yang B, Wang X, Chen X and Yang C 2014 MEMS-based ultrasonic transducer as the receiver for wireless power supply of the implantable microdevices *Sensors Actuators, A Phys.* **219** 65–72

[15] Ihlenburg F 1998 *Finite Element Analysis of Acoustic Scattering* (New York: Springer) (https://doi.org/10.1007/b98828)

[16] SimuTech Acoustic simulation of a silencer *ANSYS Tips & Tricks* [Online]. Available: (https://simutechgroup.com/tips-and-tricks/fea-articles) [Accessed: 12-Jun-2017]

[17] Sherrit S, Leary S P, Dolgin B P and Bar-Cohen Y 1999 Comparison of the Mason and KLM equivalent circuits for piezoelectric resonators in the thickness mode *1999 IEEE Ultrasonics Symp. Proc. Int. Symp. (Cat. No.99CH37027)* vol. 2 pp 921–6

[18] Prasad S A N, Gallas Q, Horowitz S B, Homeijer B D, Sankar B V, Cattafesta L N and Sheplak M 2006 Analytical electroacoustic model of a piezoelectric composite circular plate *AIAA J.* **44** 2311–8

[19] Deshpande M and Saggere L 2007 An analytical model and working equations for static deflections of a circular multi-layered diaphragm-type piezoelectric actuator *Sensors Actuators* **136** 673–89

[20] Bozkurt A 2008 A lumped-circuit model for the radiation impedance of a circular piston in a rigid baffle *IEEE Trans. Ultrason. Ferroelectr. Freq. Control* **55** 2046–52

[21] Aarts R M and Janssen A J E M 2003 Approximation of the Struve function H1 occuring in impedance calculations *J. Acoust. Soc. Am.* **113** 2635–7